Pergamon

Int. J. Heat Mass Transfer. Vol. 39, No. 17, pp. 3667–3683, 1996

0017–9310/96 $15.00 + 0.00

PII: S0017–9310(96)00031–2

Experimental observation and conjugated heat transfer analysis of vortex flow development in mixed convection of air in a horizontal rectangular duct

W. L. LIN, Y. T. KER and T. F. LIN†

Department of Mechanical Engineering, National Chiao Tung University, Hsinchu, Taiwan, Republic of China

(*Received* 18 *September* 1995 *and in final form* 27 *December* 1995)

Abstract—A combined flow visualization and conjugated heat transfer analysis was carried out to study the axial evolution of the buoyancy induced secondary vortex flow in a mixed convective air flow through a bottom heated horizontal rectangular duct. In the experiment the cross plane secondary flow was visualized at selected cross-sections. While in the conjugated analysis, the unsteady three-dimensional Navier–Stokes and energy equations for the flow were coupled with the unsteady two-dimensional conduction equations for the solid walls and were solved together numerically. Results were obtained for the Reynolds number ranging from 35 to 102 and Grashof number from 1600 to 5.8×10^5, covering the steady and time periodic flows. Both the experimental and numerical results clearly showed the generation of the longitudinal vortex rolls in the entry half of the duct and the merge of these rolls downstream. At higher buoyancy-to-inertia ratio more rolls were generated and they merged into fewer and larger rolls. Significant conjugated heat transfer effects were noted from the numerical results. Copyright © 1996 Elsevier Science Ltd.

1. INTRODUCTION

The understanding of the complex temporal and spatial structures of the buoyancy induced secondary vortex flow in a low Reynolds number and high Grashof number forced convective gas flow through a bottom heated horizontal duct, is important in fundamental fluid mechanics and heat transfer study, and in various technological applications such as design of compact heat exchangers and growth of single crystal thin film by chemical vapor deposition (CVD). In a series of studies [1–3] the present authors carried out numerical simulation and experimental measurement to unravel these complex flow characteristics in an air flow through a bottom heated horizontal rectangular duct of aspect ratio $A = 2$ and 4. The formation, merging and splitting of the longitudinal vortex rolls were numerically predicted for the laminar steady, laminar time periodic, transitional quasiperiodic and irregular chaotic flow at increasing buoyancy and/or decreasing inertia forces [1, 2]. The flow visualization [3] at a given downstream cross-section near the duct exit and the time records of the air temperature at a number of selected locations qualitatively supported the numerical predictions. However, noticeable differences in the vortex roll structures between the numerical and experimental studies do exist. These differences were found to mainly result from the conjugated effects of the air convection in the duct and the conduction in the side walls in view of the fact that the thermal conductivity of the plexiglass side walls is much higher than that of air. These conjugated heat transfer effects were ignored in the numerical predictions. To complement the above studies, the present investigation intends to experimentally visualize the axial development of the roll structures in an air flow through a bottom heated horizontal rectangular duct with the aspect ratio A fixed at 4, and to account for the conjugated effects in the numerical simulation.

A detailed account of the literature on the mixed convection in a horizontal rectangular duct has been given in our previous study [1]. Only the recent literature relevant to the topic is briefly reviewed in the following.

The onset of thermal instability and the associated heat transfer enhancement in a bottom heated horizontal plane channel were found to occur at $Ra = 1708$ [4–6]. Beyond this critical Rayleigh number, steady longitudinal vortex rolls prevail. In the mixed convection of nitrogen gas, Rosenberger and his coworkers [7, 8] observed the unsteady snaking longitudinal vortex rolls even for the Rayleigh number only slightly above the critical value of 1708. Besides, the asymmetric roll patterns were also found at low Rayleigh numbers. A flow regime map of Re vs Ra was proposed to predict the boundaries among the flow with no roll, steady and unsteady rolls. Finally, the transverse rolls were noted at very low

† Author to whom correspondence should be addressed.

NOMENCLATURE

A aspect ratio, b/d
b, d width and height of the duct
g gravitational acceleration
Gr modified Grashof number, $g\beta q''_{conv}d^4/kv^2$
Gr_z local Grashof number $g\beta q''_{conv}z^4/kv^2$
Gz Graetz number, $d\cdot Re\cdot Pr/z$
h local convection heat transfer coefficient
k thermal conductivity
l, L dimensional and dimensionless length of the heated plate, l/d
M volume flow rate
Nu Nusselt number, hd/k
p_m, P dimensional and dimensionless dynamic pressures, $p_m/\rho\bar{w}_{in}^2$
Pr Prandtl number, v/α
q''_{conv} local convective heat flux
q''_{insul} local conduction heat loss through the insulation
q''_{loss} local heat loss, $q''_{rad}+q''_{insul}$
q''_{rad} local radiation heat loss from the surface
q''_{tot} the total heat flux in the plate
q''_w wall heat flux
$\dot{q}'''$ volumetric heat source
Ra Rayleigh number
Re Reynolds number, $\bar{w}_{in}d/v$
Re_z local Reynolds number, $\bar{w}_{in}z/v$
t, τ dimensional and dimensionless time, $t/(d/\bar{w}_{in})$
T, θ dimensionless and dimensionless temperature, $(T-T_{in})/(q''_w d/k)$
T_{avt} time-average temperature at a given location
u, v, w velocity components in x, y, z directions
U, V, W dimensionless velocity components, in X, Y, Z directions, $u/\bar{w}_{in}$, $v/\bar{w}_{in}$ and $w/\bar{w}_{in}$
x, y, z Cartesian coordinates
X, Y, Z dimensionless Cartesian coordinates, x/d, y/d, and z/d
Z^* modified Z coordinate, $z/d\cdot Re\cdot Pr$.

Greek symbols
α thermal diffusivity
β thermal expansion coefficient
δ thickness
v kinematic viscosity
ρ density
σ Stefan–Boltzmann constant.

Subscripts
a of ambient quantities
fd fully developed
in values at the inlet of the test section
lon of Superlon insulator quantities
p period
s of plexiglass plate quantities
s–f values from plexiglass plate to fluid
s–w values from plexiglass plate to heater plate
side of side wall quantities
t of top wall quantities
w of heated wall quantities
w–f values from heater plate to fluid
w–s values from heater plate to plexiglass plate.

Superscripts
$\bar{}$ average value.

Reynolds number by Ouazzani *et al.* [9, 10]. They also refined the regime map to include the transverse rolls.

A series of experiments conducted by Incropera and his coworkers [11–13] showed the onset and qualitative picture of the buoyancy driven secondary flow on the bottom plate. Their flow visualization distinctly discloses four flow regimes along the bottom plate—laminar forced convection, laminar mixed convection, transitional mixed convection and turbulent free convection. The transition to turbulent flow was attributed to the breakdown of the vortices due to the hydrodynamic instability [13]. Various numerical works [14–18] were recently carried out based on the assumption that the axial viscous and thermal diffusion can be neglected, i.e. the flow is parabolic and thus, the problem can be solved efficiently by various marching techniques. In view of the presence of the three-dimensional transient transitional flow in the duct, this approximation becomes inappropriate at high Rayleigh or low Reynolds numbers.

In the following, the experiment designed to study the axial development of the vortex flow structures and the flow transition will be described first. Then, the numerical model and solution procedures used to calculate the conjugated mixed convection observed in the experiment will be discussed. Finally, the experimental and numerical results will be examined in detail.

2. EXPERIMENTAL APPARATUS AND PROCEDURES

2.1. *Experimental apparatus*

Figure 1 shows a schematic view of the mixed convective experimental apparatus established in the pre-

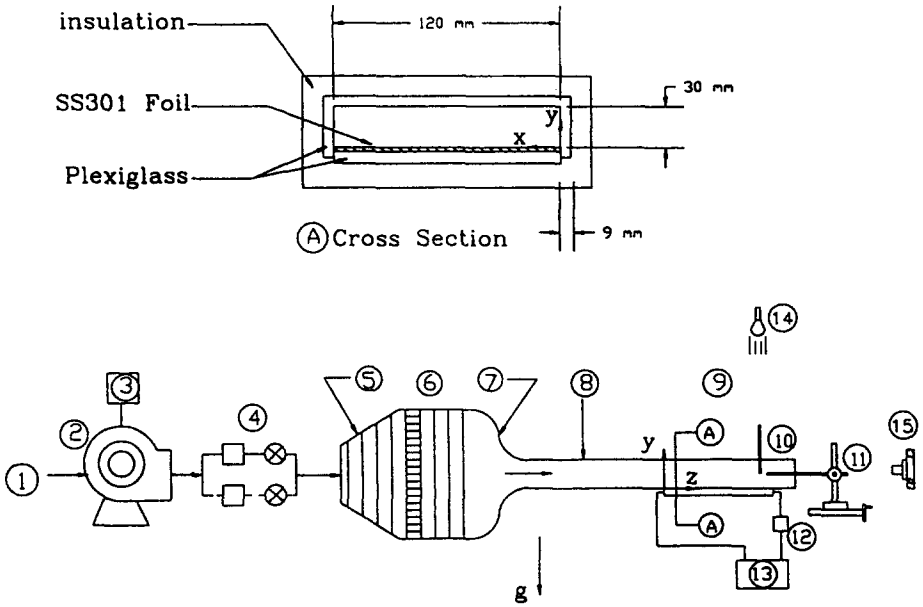

Schematic Diagram of Experimental Apparatus.

1.air flow ; 2.blower ; 3.frequency regulator ; 4.flowmeters and valves ; 5.diffuser with screens ; 6.straightener with honeycomb and screens ; 7.nozzle ; 8.developping chanel ; 9.test section ; 10.probes ; 11.three-way traversing device ; 12.ammeter ; 13. D.C. power supply ; 14.lamp ; 15.camera.

Fig. 1. The schematic diagram of the experimental apparatus.

vious study [3] and also used here. The apparatus consists of three parts: wind tunnel, test section and measuring probes along with the data acquisition system. The test section is a bottom heated rectangular duct constructed of 9 mm thick plexiglass top and side walls to facilitate flow visualization. The duct is rectangular, 30 mm in height and 120 mm in width, providing an aspect ratio of $A = 4$ and a total length of $l = 800$ mm. Its bottom wall was made of 0.25 mm thick SS301 stainless steel heater plate and was bonded on to a sheet of 12 mm thick plexiglass plate. Direct electric current was provided from a 30 V-50 A d.c. power supply and transferred to the heater plate through several copper bus-bars firmly attached at the ends of the heater plate, intending to produce a nearly uniform heat flux boundary condition. Power dissipation was determined by measuring the current and voltage drop across the heater plate and uniformity of the energy dissipation was checked by measuring the voltage distribution on the plate. The entire channel, including the test section and the upstream and downstream flow straighteners, was insulated with a 150 mm thick Superlon insulator and mounted on a rigid supporting frame.

Air was driven by a blower and sent into the long rectangular duct downstream of a diffuser buffer section, as shown in Fig. 1. The air flow rate upstream of the diffuser buffer section was measured by a float-area-type flowmeter with an accuracy of 1.6%. To reduce the influence of the vibration from the blower, a flexible connection made of cloth was used to connect the blower and a diffuser buffer section. The purpose of installing the diffuser buffer section and a series of three additional fine-mesh screens was to reduce turbulence from the blower blades. In the inlet section, turbulence was further suppressed by passing the air through a section packed with plastic straws of 3 mm in diameter and bounded on each side by two fine mesh screens, and then followed by a nozzle and a developing channel, before entering the test section. The nozzle is made of 5 mm thick acrylic plate with a contraction ratio of 10 : 1, and has been designed to eliminate flow separation, minimize turbulence, and provide a nearly uniform velocity profile at the inlet of the developing section. The developing section is 1000 mm in full length, approximately 33 times the duct height. This insures the flow being fully developed at the inlet of the test section for $Re \leqslant 200$. The optical observations of the flow structure were performed using smoke tracers to determine the pattern of the secondary flow. A thin sheet of smoke was injected into the test section along the bottom of the channel, through a slot across the width of the heater plate just in front of the test section. When illuminated

through the top wall by lamps and viewed from the end of the channel, a sharp contrast could be achieved between the channel walls and the smoke.

In order to obtain adequate resolution of the temperature distributions on the bottom wall, the heater plate was instrumented with 57 (placed at 19 longitudinal locations) calibrated copper–constantan (T-type) thermocouples and their signals were recorded by the Hewlett-Packard 3852A data acquisition system with a resolution of ± 0.05 C. Additional thermocouples were used to measure the temperatures of the inlet and outlet air flow and the top and side plates and to determine temperature differences across the Superlon insulation underneath the heater plate. A T-type thermocouple having a bead of 70 μm diameter was used to measure the air temperature in the duct, which was equipped in the flow so as to have its sensing point 5 mm upstream of the supporting stainless steel pipe of 1 mm outer diameter. This probe was inserted into the flow through the top wall or from the exit end of the channel and can be traversed in the flow to measure the time-averaged temperature field and the instantaneous temperature. The temperature data are recorded when the system reaches steady or statistical state, usually 5–6 h after starting the test. The experiment was performed mainly at the Grashof numbers ranging from 1.6×10^3 to 5.8×10^5 and for the Reynolds numbers below 102.

2.2. *Data reduction for convective heat transfer*

The surface energy balance relating the total energy dissipated in the thin heater plate due to the resistance heating per unit surface area q''_{tot} to the heat fluxes associated with the convection from the heated surface to the air flow q''_{conv}, radiaiton heat loss from the surface q''_{rad} and conduction loss through the insulation q''_{insul} is

$$q''_{tot} = q''_{conv} + q''_{rad} + q''_{insul}. \tag{1}$$

The convective heat flux was therefore determined by measuring the total dissipated heat flux and applying appropriate correlations for the nonconvective components.

Considering the shape factor and surface resistances for thermal radiation from the heated bottom surface to the top plate and to the two side plates, the net radiation loss from the bottom surface was estimated as

$$q''_{rad} = 0.331\sigma(\bar{T}_w^4 - \bar{T}_t^4) + 2 \times 0.082\sigma(\bar{T}_w^4 - \bar{T}_{side}^4) \tag{2}$$

with the mean temperature of the heated surface $\bar{T}_w$ measured directly and the mean top and side plate temperatures $\bar{T}_t$ and $\bar{T}_{side}$ obtained by interpolation between the measured values.

Conduction losses through the insulation q''_{insul} were calculated by assuming one-dimensional conductive transfer and by measuring the temperature difference across the first 9 mm of the insulation ($k_{insul} = 0.21$ W m^{-1} °C^{-1}) beneath the heater plate,

$$q''_{insul} = -k_{insul} \left.\frac{\Delta T}{\Delta y}\right|_{insul}. \tag{3}$$

2.3. *Analysis of temperature fluctuation*

The time-averaged temperature and the intensity of the temperature fluctuation of the air flow were obtained by averaging 1000 sampled data at each detection point. In the tests the detection points are distributed at 24 equi-spaced spanwise positions in the horizontal planes at $y = 5$, 15 and 25 mm. Also, the power spectrum densities of the temperature fluctuation were obtained by analyzing the output of the thermocouple using a FFT analyzer.

3. MATHEMATIC MODEL AND SOLUTION METHOD

3.1. *Geometry*

The physical model employed to simulate the mixed convective air flow in a bottom heated horizontal rectangular duct with finite thickness walls is shown in Fig. 2, along with the chosen coordinate system. An isothermal fully developed forced flow at temperature T_{in} and averaged speed $\bar{w}_{in}$ enters the duct at the upstream of the heated section. Initially, the flow in the entire duct is isothermal at T_{in}. At a certain instant of time, designated as time $t = 0$, a uniform volumetric heat source $\dot{q}'''$ is suddenly generated by the resistance heating in the thin heater plate and is maintained at this level thereafter. Meanwhile, the entire duct is thermally well insulated by the Superlon insulator. Note that two thermally well insulated sections of length L and $L/2$ are, respectively, added to the upstream and downstream ends of the heated section to facilitate the prescription of the in-flow and out-flow boundary conditions in the present elliptic flow analysis.

3.2. *Governing equations*

Basic nondimensional equations describing this unsteady mixed convective flow of a Boussinesq fluid in a bottom heated horizontal rectangular duct driven by the interactions of the convection in the duct and conduction in the duct walls are

(*a*) *Convection equations for flow in the duct.*

Continuity equation

$$\frac{\partial U}{\partial X} + \frac{\partial V}{\partial Y} + \frac{\partial W}{\partial Z} = 0 \tag{4}$$

X-direction momentum equation

$$\frac{\partial U}{\partial \tau} + U\frac{\partial U}{\partial X} + V\frac{\partial U}{\partial Y} + W\frac{\partial U}{\partial Z} = -\frac{\partial P}{\partial X} + \frac{1}{Re}\left[\frac{\partial^2 U}{\partial X^2} + \frac{\partial^2 U}{\partial Y^2} + \frac{\partial^2 U}{\partial Z^2}\right]. \tag{5}$$

Y-direction momentum equation

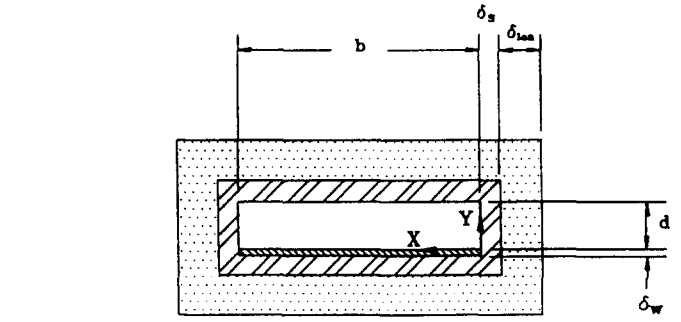

Cross Section of Heating Region

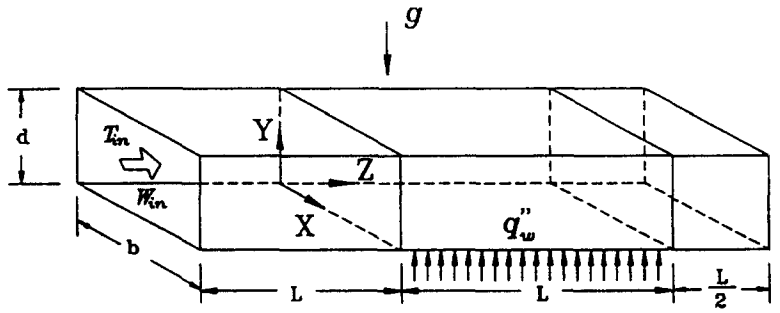

The Physical System of Numerical Model

Fig. 2. The physical system of the numerical model for a mixed convective air flow in a rectangular duct.

$$\frac{\partial V}{\partial \tau}+U\frac{\partial V}{\partial X}+V\frac{\partial V}{\partial Y}+W\frac{\partial V}{\partial Z}=-\frac{\partial P}{\partial Y}+\frac{1}{Re}\left[\frac{\partial^2 V}{\partial X^2}+\frac{\partial^2 V}{\partial Y^2}+\frac{\partial^2 V}{\partial Z^2}\right]+\frac{Gr}{Re^2}\theta. \quad (6)$$

Z-direction momentum equation

$$\frac{\partial W}{\partial \tau}+U\frac{\partial W}{\partial X}+V\frac{\partial W}{\partial Y}+W\frac{\partial W}{\partial Z}=-\frac{\partial P}{\partial Z}+\frac{1}{Re}\left[\frac{\partial^2 W}{\partial X^2}+\frac{\partial^2 W}{\partial Y^2}+\frac{\partial^2 W}{\partial Z^2}\right]. \quad (7)$$

Energy equation

$$\frac{\partial \theta}{\partial \tau}+U\frac{\partial \theta}{\partial X}+V\frac{\partial \theta}{\partial Z}+W\frac{\partial \theta}{\partial Z}=\frac{1}{Re\cdot Pr}\left[\frac{\partial^2 \theta}{\partial X^2}+\frac{\partial^2 \theta}{\partial Y^2}+\frac{\partial^2 \theta}{\partial Z^2}\right]. \quad (8)$$

Nondimensional variables used in the above equations are defined in the following:

$$X=x/d \quad Y=y/d \quad Z=z/d$$

$$U=u/\bar{w}_{in} \quad V=v/\bar{w}_{in} \quad W=w/\bar{w}_{in}$$

$$\tau=t/(d/\bar{w}_{in}) \quad P=p_m/\rho\bar{w}_{in}^2 \quad \theta=(T-T_{in})/(q''_w d/k)$$

$$Gr=g\beta q''_w d^4/kv^2 \quad Pr=v/\alpha \quad Re=\bar{w}_{in}d/v \quad A=b/d,$$

where q''_w is the wall heat flux and is considered to be equal to $\bar{q}''_{conv}$ determined by averaging the data from the experimental measurement, equation (1).

(*b*) *Conduction equations in the solid walls.* Considering that the thickness of the duct wall is much smaller than its length and width, the conduction resistance across the wall is neglected here to facilitate the computation. Thus we have equations for

the heater plate

$$\frac{\partial \theta_w}{\partial \tau}=\left(\frac{\alpha_{rw}}{Pr\cdot Re}\right)\left\{\left(\frac{\partial^2 \theta_w}{\partial X^2}+\frac{\partial^2 \theta_w}{\partial Z^2}\right)-\left(\frac{k_{rs}}{k_{rw}}\right)\left(\frac{d}{\delta_w}\right)\times\left[\frac{\theta_w-\theta_s}{(\delta_w+\delta_s)/2d}\right]+\left(\frac{1}{k_{rw}}\right)\left(\frac{d}{\delta_w}\right)\left(1+\frac{\partial \theta}{\partial Y}\Big|_{w\text{-}f}\right)\right\} \quad (9)$$

the plexiglass bottom wall

$$\frac{\partial \theta_s}{\partial \tau}=\left(\frac{\alpha_{rs}}{Pr\cdot Re}\right)\left\{\left(\frac{\partial^2 \theta_s}{\partial X^2}+\frac{\partial^2 \theta_s}{\partial Z^2}\right)-\left(\frac{k_{rlon}}{k_{rs}}\right)\left(\frac{d}{\delta_s}\right)\left(\frac{\theta_s-\theta_a}{\delta_{lon}/d}\right)+\left(\frac{d}{\delta_s}\right)\left[\frac{\theta_w-\theta_s}{(\delta_w+\delta_s)/2d}\right]\right\} \quad (10)$$

the plexiglass right side wall

$$\frac{\partial\theta_s}{\partial\tau}=\left(\frac{\alpha_{rs}}{Pr\cdot Re}\right)\left[\left(\frac{\partial^2\theta_s}{\partial Y^2}+\frac{\partial^2\theta_s}{\partial Z^2}\right)-\left(\frac{1}{k_{rs}}\right)\left(\frac{d}{\delta_s}\right)\frac{\partial\theta}{\partial X}\bigg|_{s\text{-}f}-\left(\frac{k_{rlon}}{k_{rs}}\right)\left(\frac{d}{\delta_s}\right)\left(\frac{\theta_s-\theta_a}{\delta_{lon}/d}\right)\right] \quad (11)$$

the plexiglass left side wall

$$\frac{\partial\theta_s}{\partial\tau}=\left(\frac{\alpha_{rs}}{Pr\cdot Re}\right)\left[\left(\frac{\partial^2\theta_s}{\partial Y^2}+\frac{\partial^2\theta_s}{\partial Z^2}\right)+\left(\frac{1}{k_{rs}}\right)\left(\frac{d}{\delta_s}\right)\frac{\partial\theta}{\partial X}\bigg|_{s\text{-}f}-\left(\frac{k_{rlon}}{k_{rs}}\right)\left(\frac{d}{\delta_s}\right)\left(\frac{\theta_s-\theta_a}{\delta_{lon}/d}\right)\right] \quad (12)$$

the plexiglass top wall

$$\frac{\partial\theta_s}{\partial\tau}=\left(\frac{\alpha_{rs}}{Pr\cdot Re}\right)\left[\left(\frac{\partial^2\theta_s}{\partial X^2}+\frac{\partial^2\theta_s}{\partial Z^2}\right)-\left(\frac{1}{k_{rs}}\right)\left(\frac{d}{\delta_s}\right)\frac{\partial\theta}{\partial Y}\bigg|_{s\text{-}f}-\left(\frac{k_{rlon}}{k_{rs}}\right)\left(\frac{d}{\delta_s}\right)\left(\frac{\theta_s-\theta_a}{\delta_{lon}/d}\right)\right]. \quad (13)$$

Note that in writing the above equations, the outside surface of the Superlon insulator is assumed at the ambient temperature, which is the same as the inlet temperature in the present experiment. Besides, the thermal diffusivity and conductivity ratios and wall thickness are defined and assigned with the values for the present system as

$$\alpha_{rs}=\alpha_s/\alpha\approx 0.00553,\quad \alpha_{rw}=\alpha_w/\alpha\approx 0.187$$

$$k_{rs}=k_s/k\approx 7.622,\quad k_{rw}=k_w/k\approx 571.43,$$

$$k_{rlon}=k_{lon}/k\approx 10,\quad d/\delta_s\approx 3.333,$$

$$d/\delta_w\approx 120,\quad \delta_{lon}/d\approx 5.$$

Due to the neglect of the thermal resistance across the thickness of the walls, the solution from the above conduction equations actually acts as the thermal boundary conditions for the flow equations.

(*c*) *Initial and boundary conditions.* The imposed initial and boundary conditions of the above governing equations are

at $\tau\leqslant 0$, $U=V=\theta=\theta_w=\theta_s=0$

$$W=W_{fd}=\left(\frac{m+1}{m}\right)\left(\frac{n+1}{n}\right)[1-(|2Y-1|)^n]\times\left[1-\left(\left|\frac{2X}{A}-1\right|\right)^m\right], \quad (14)$$

where the initial velocity is assumed as fully developed with the values of the constants m and n depending on the aspect ratio A [19].

$$\text{At } \tau>0,\quad \text{at } Z=-L, \quad (15)$$

$$U=V=\theta=\theta_s=0,\quad W=W_{fd}$$

$$\text{at } Z=\frac{3L}{2},\quad \frac{\partial U}{\partial Z}=\frac{\partial V}{\partial Z}=\frac{\partial W}{\partial Z}=\frac{\partial\theta}{\partial Z}=\frac{\partial\theta_s}{\partial Z}=0 \quad (16)$$

$$\text{at } Z=0 \quad \text{and} \quad L,\quad \frac{\partial\theta_w}{\partial Z}=0 \quad (17)$$

at the fluid–wall interfaces,

$$U=V=W=0,\quad \theta=\theta_s \quad \text{or} \quad \theta=\theta_w. \quad (18)$$

3.3. *Solution method*

In view of the nonlinearity in the inertia terms, the basic equations were solved numerically. In particular, the explicit finite-difference method was used to solve the conduction equations in the solid walls. Meanwhile, the explicit projection method [20] was chosen to integrate the flow equations on a staggered grid system. This fractional step (splitting) method consists of two steps. First, a provisional value is explicitly computed for the velocity field ignoring the pressure gradient. Then, the provisional velocity field is corrected by including the pressure effect and by enforcing the mass conservation.

To enhance the numerical accuracy and stability, a third-order upwind scheme developed by Kawamura *et al.* [21] is adopted to discretize the convective terms. Additionally, the diffusive terms are approximated by a fourth-order central difference [22].

The sequence of numerical operation for advancing a time step is as follows:

(1) Explicitly calculate the provisional velocity field.

(2) Solve the Poisson equation for pressure. Solution for the pressure is considered as convergent when the mean relative pressure difference between two consecutive iterations is below 5×10^{-4}. This insures the mass imbalance at each node is less than 10^{-4} of the inlet mass flowrate.

(3) Explicitly calculate the corrected velocity field at the new time step.

(4) Explicitly calculate the temperature fields in the flow and in the solid walls at the new time step.

In view of the symmetry in the flow and thermal conditions with respect to the center vertical plane at $X=A/2$, only the left or right half domain should be used in the computation. However, the symmetry of the flow may be broken when the flow becomes oscillatory in time at high buoyancy. Thus the entire domain is used in the computation to allow for the possible presence of the asymmetric flow.

Since only the low Reynolds number flow ($Re\leqslant 102$) is to be simulated, a uniform grid is placed in the computational domain with $\Delta X=A/I$, $\Delta Y=1/J$ and $\Delta Z=2.5L/K$ where I, J and K are, respectively, the total numbers of nodes used in the X, Y and Z directions. I, J and K are, respectively, chosen as 61, 22 and 91. The stability of the scheme is limited by the requirement that the Courant number be less than unity [23]. To ensure numerical convergence and enhance numerical accuracy, the Courant number is set below 0.05 in the computation.

To verify the proposal numerical scheme, a series of stringent program tests were conducted. First, the predicted results for the flow without considering the wall conduction effects were in qualitative agreement with the results in literature, as was clearly illustrated in our previous numerical study [1]. Then, the present predictions including the conjugated heat transfer effects are compared with the present experimental results. A small sample of the results is given in Fig. 3 for $Re = 51$ and 102 for various Grashof numbers.

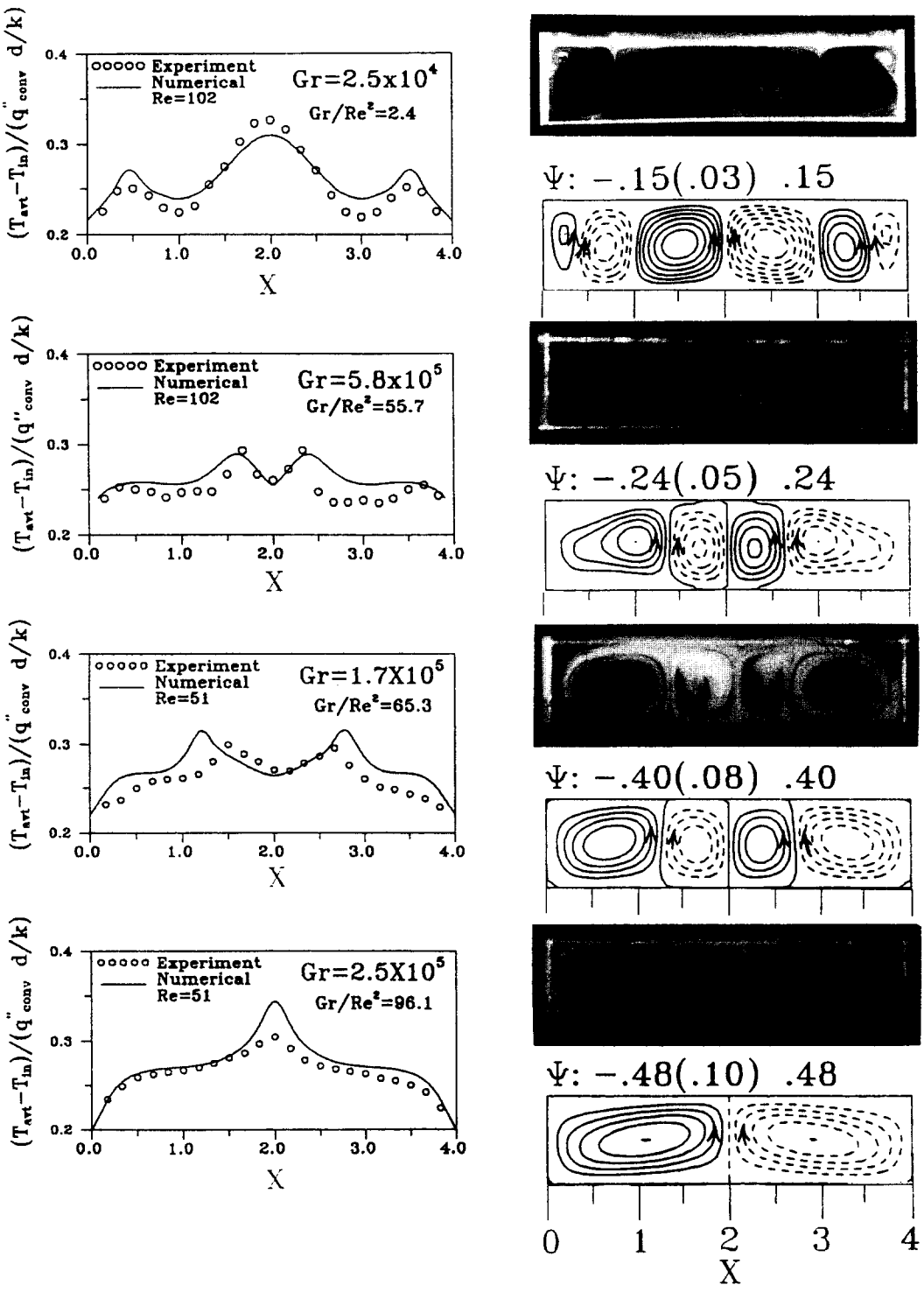

Fig. 3. Comparisons of experimental and computed results for $Re = 51$ and 102 at $z = 0.7$ m ($Z \approx 23.3$, $Z^* \approx 0.64$ for $Re = 51$ and 0.32 for $Re = 102$) and $Y = 0.5$ at large τ.

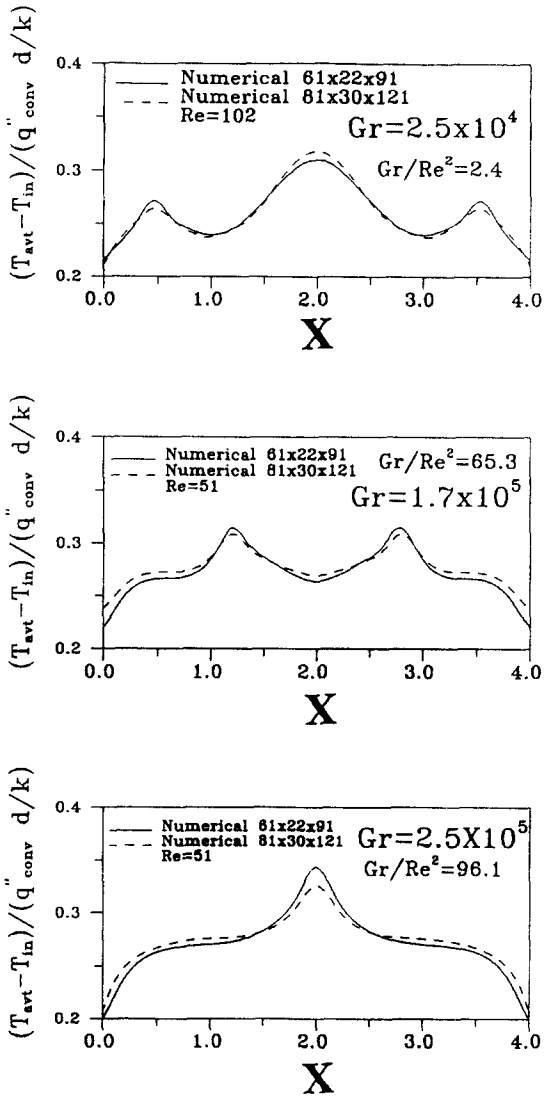

Fig. 4. Comparison of the predicted time-averaged spanwise temperature distributions at large τ from various grids for various Grashof numbers for $Re = 51$ and 102 at $z = 0.7$ m ($Z \approx 23.3$, $Z^* \approx 0.64$ for $Re = 51$ and $Z^* \approx 0.32$ for $Re = 102$) and $Y = 0.5$.

Note that the predicted time-average temperature distribution T_{avt} in the spanwise direction at $y = d/2$ and the cross plane vortex flow structures at $z = 0.7$ m agree reasonably with the experimental results. More comparison will be made later between the present numerical simulation and experimental measurement. Furthermore, a grid-independence test was carried out. Sampled results from such tests for the spanwise distributions of T_{avt} are shown in Fig. 4 at $y = d/2$ and $z = 0.7$ m for three different cases computed by the grids $61 \times 22 \times 91$ and $81 \times 30 \times 121$. Note that the differences in these calculated from these two grids are less than 5%. Through these program tests the adopted solution procedures are considered to be suitable for the present study. Finally, it should be mentioned that the computations were performed on the IBM 580 workstations. The CPU times for these unsteady fully three-dimensional cases were about 4–8 days with a 50% share of CPU. Due to the limited availability of the computational facilities, grids much larger than those used above were not tested.

4. RESULTS AND DISCUSSIONS

In the following, selected results from the present experimental and numerical investigation will be presented to mainly illustrate the axial development of the buoyancy induced vortex flow structures for various Reynolds and Grashof numbers. Then the conjugated heat transfer effects are manifested.

4.1. *Axial evolution of vortex flow*

At low buoyancy-to-inertia ratio (Gr/Re^2) steady vortex flow prevails after the transient has elapsed when the Grashof number is above the critical value for the onset of secondary flow. To exemplify this vortex flow development, Fig. 5 shows the photos of the steady secondary flow at selected cross-sections for $Re = 102$ and $Gr/Re^2 = 2.4$ ($Gr = 24970$). For clear comparison, the corresponding secondary flow and isotherms from the conjugated heat transfer analysis are also shown in Fig. 5. Note that the vortex flow development visualized from the experiment is in good agreement with that from the numerical simulation. These results indicate that in the immediate entry of the heated section one pair of vortices are induced near the side walls. This cross plane secondary flow rises from the bottom heated plate along the side walls. When the flow moves downstream, another pair of vortices form in the core region adjacent to the first pair, as evident from the photo for $z = 0.4$ m ($Z \approx 13.3$). The isotherms suggest that these newly formed vortex rolls are driven by the thermal rising from the central portion of the heated plate. Thus we have two pairs of longitudinal vortex rolls in the duct, which are symmetric with respect to the vertical central plane at $X = 2$. Further downstream the rolls in the duct core grow slightly in size and strength. This in turn squeezes the rolls near the side walls to become smaller. As the flow moves still forwards to $z \approx 0.6$ m ($Z \approx 20$), the rolls near the duct sides shrink noticeably near the upper corners and another pair of smaller vortices appear in these regions. These corner vortices gradually grow along the duct sides as the flow approaches to the exit of the heated section. Thus, at $z = 0.7$ m ($Z \approx 23.3$) we observed one big strong pair of vortex rolls in the core, one pair of slightly smaller rolls adjacent to them and another small weak pair of rolls near the side walls. It should be noted that the rolls near the duct sides circulate downwards along the side walls. This reflects the importance of the conduction in the plexiglass side walls in the formation of the vortex rolls. Without including this wall conduction effect, the numerically predicted vortex rolls would circulate upwards near the duct sides. In summary, our results suggest that the axial evolution of

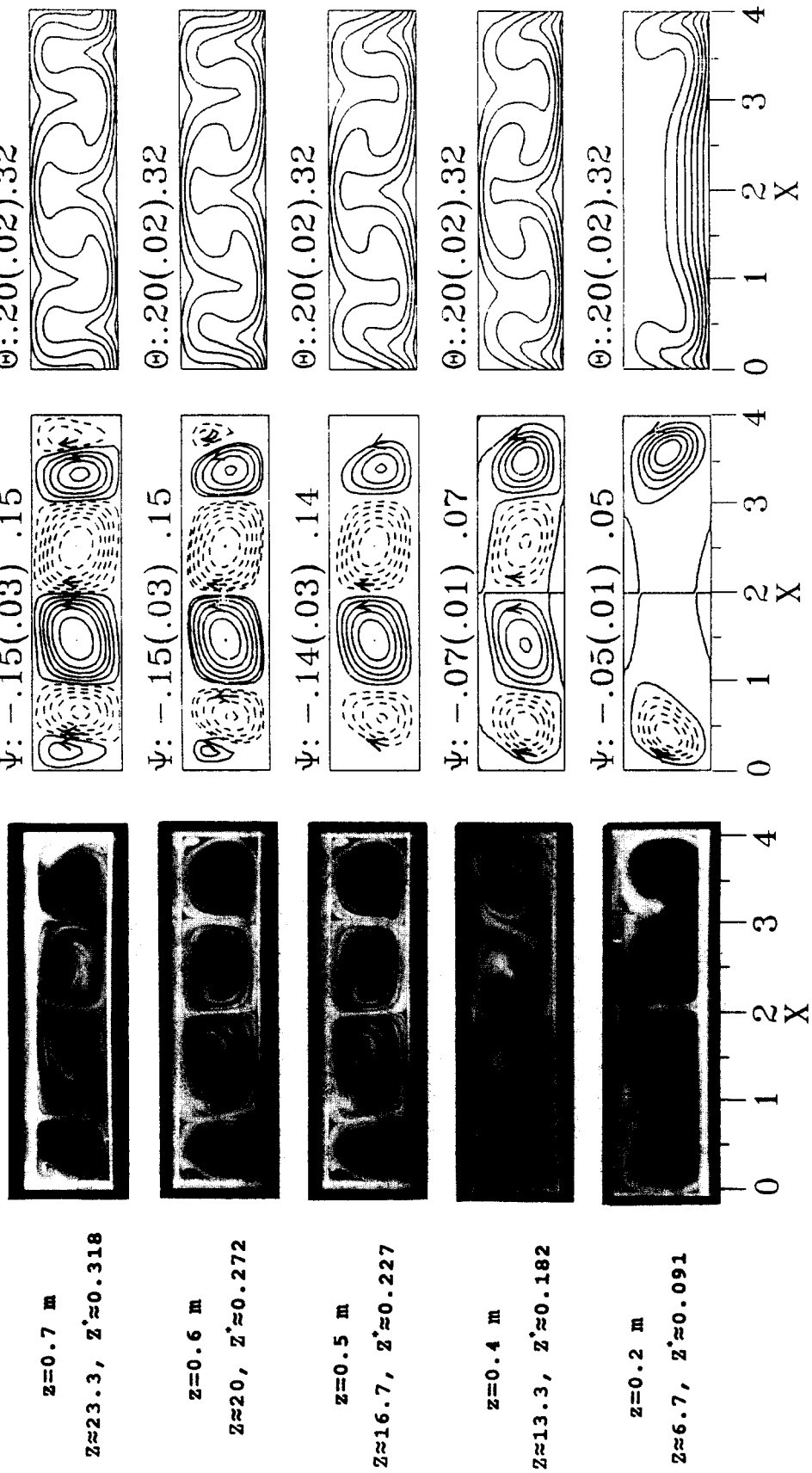

Fig. 5. (a) Experimental photos and (b) computed results at $\tau = 1200$ for air flow for $Re = 102$, $Gr/Re^2 = 2.4$ and $A = 4$ at selected cross-sections.

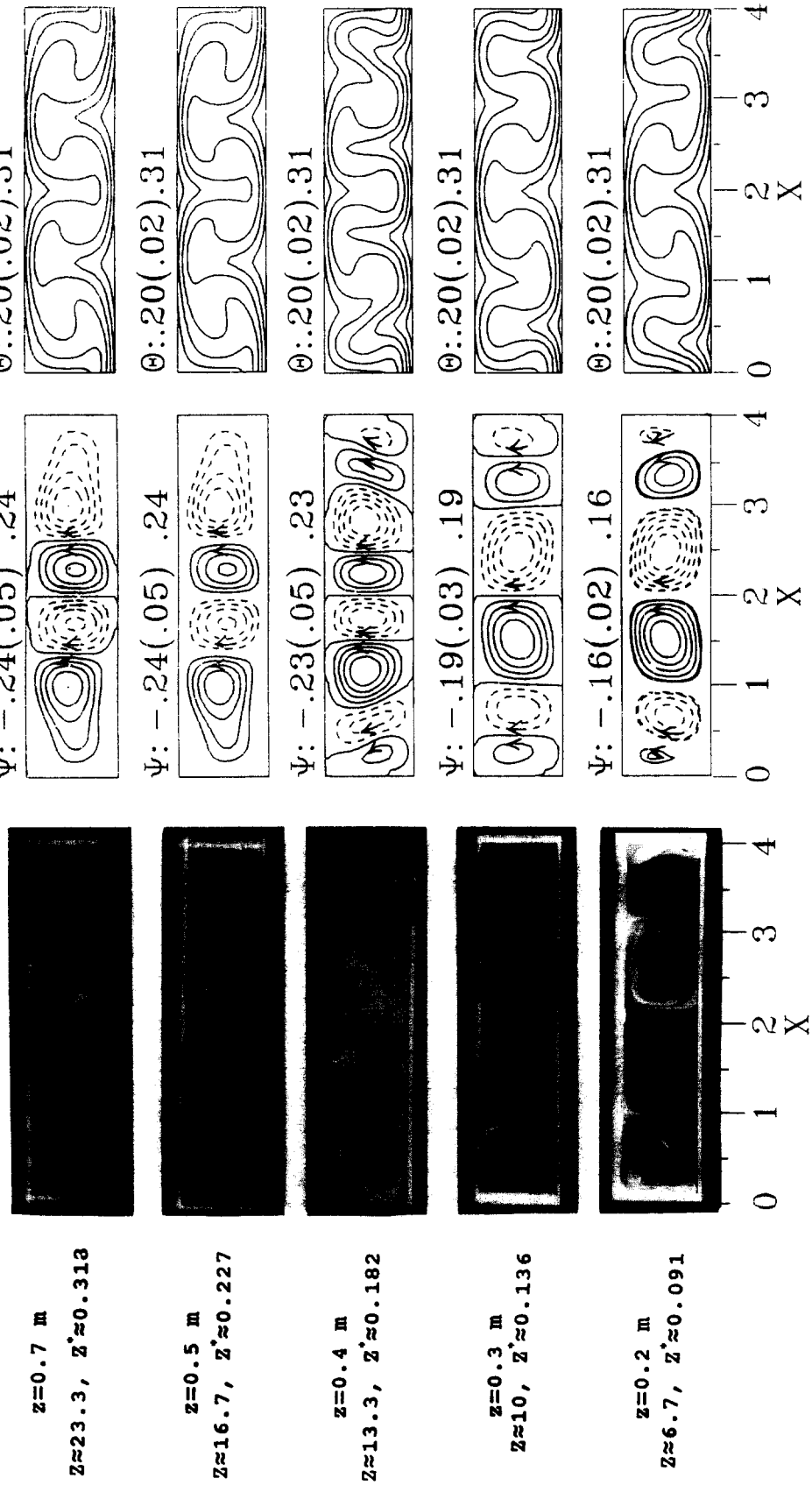

Fig. 6. (a) Experimental photos and (b) computed results at $\tau = 600$ for air flow for $Re = 102$, $Gr/Re^2 = 55.7$ and $A = 4$ at selected cross-sections.

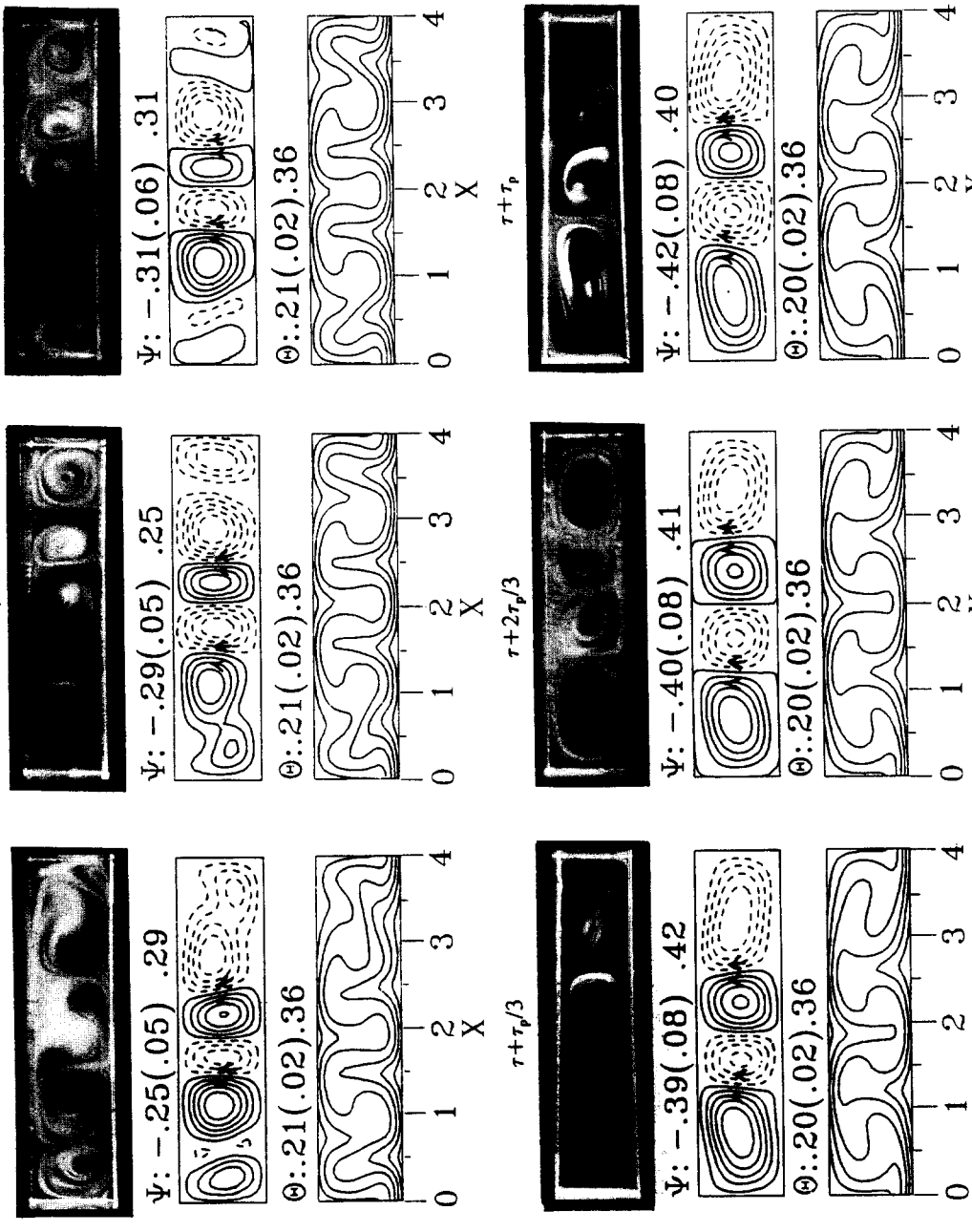

Fig. 7. The experimental and numerical instantaneous flow visualizations in a period ($\tau_p = 1.8$) for $Re = 51$ and $Gr/Re^2 = 65.3$ at (a) $z = 0.3$ m ($Z \approx 10$, $Z^* \approx 0.27$), (b) $z = 0.7$ m ($Z \approx 23.3$, $Z^* \approx 0.64$) at large τ.

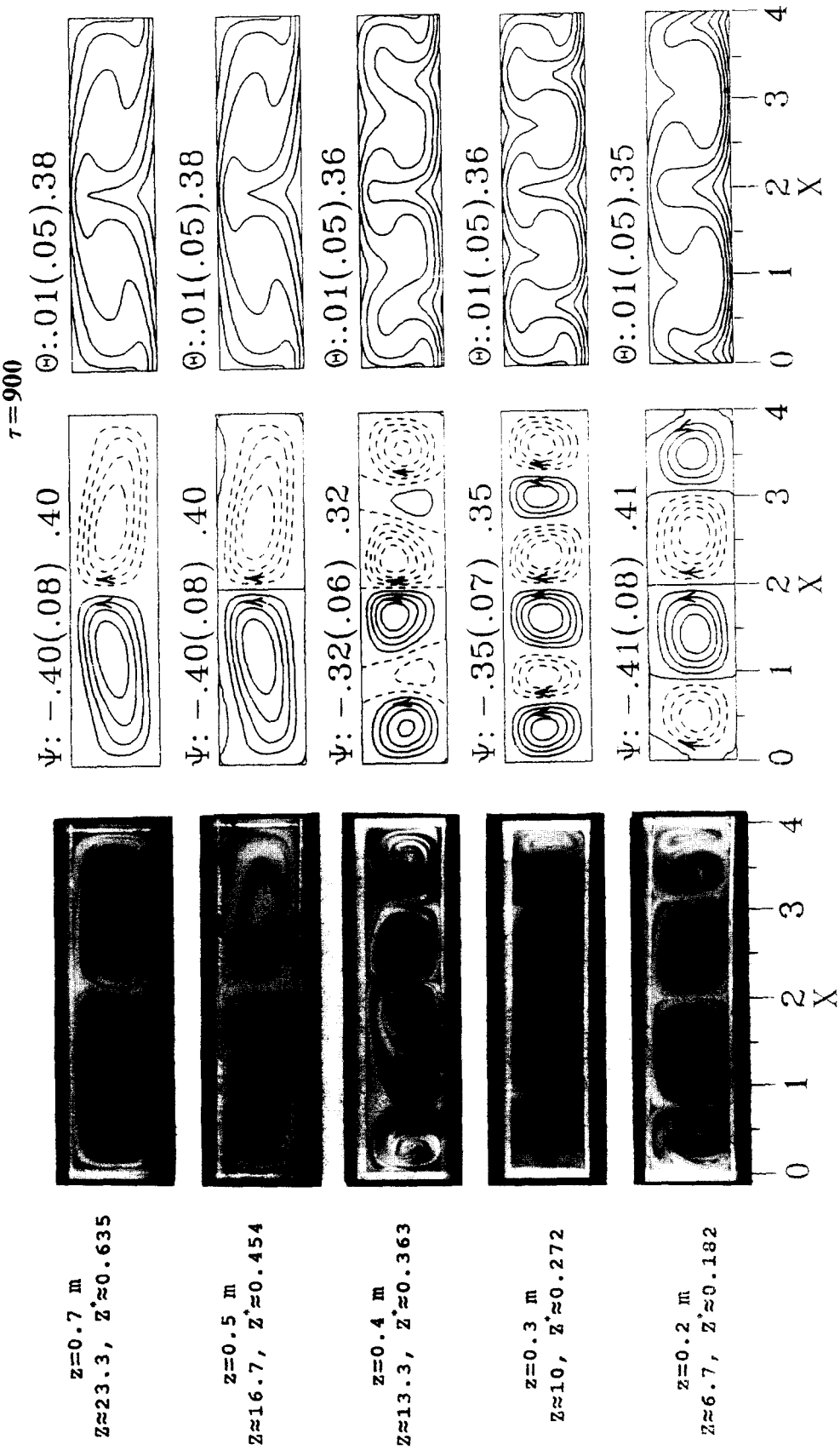

Fig. 8. (a) Experimental photos and (b) computed results at $\tau = 900$ for air flow for $Re = 51$, $Gr\,Re^2 = 96.1$ and $A = 4$ at selected cross-sections.

the vortex flow at low buoyancy is mainly characterized by the generation of symmetric vortex rolls as the flow moves downstream.

Next, the axial development of the vortex flow at the buoyancy-to-inertia ratio high enough to cause the flow to become time periodic is examined [1]. Results for a typical case are given in Fig. 6 in which a snapshot of the secondary flow at large τ at selected cross-sections is shown for $Re = 102$ and $Gr/Re^2 = 55.7$ ($Gr = 5.8 \times 10^5$). The experimental results indicate that at this higher buoyancy, three symmetric paris of longitudinal rolls have been generated in a short distance after the flow enters the heated section ($z = 0.3$ m). When the flow proceeds further downstream, the vortex rolls begin to merge together and the secondary flow is rather complicated, as is suggested by the experimental photo for $z = 0.4$ m ($Z \approx 13.3$). At $z \geqslant 0.5$ m, only two pairs of vortex rolls exist. Also note that the vortex flow is highly asymmetric during the process of the roll merging. After the merging the roll pattern is still asymmetric, but to a lower degree. The agreement between the numerical prediction and experimental observation is excellent only before the cell merging starts. But beyond that a symmetric roll pattern is predicted by the numerical calculation. This discrepancy is conjectured to result from the small random background disturbances always existing in the experiment, but not included in the computation. On the whole, at this intermediate buoyancy, new roll generation takes place in the entry portion of the duct, and downstream cell combination occurs. A similar vortex roll evolution was noted for the flow at different Reynolds numbers studied here.

In addition to the instantaneous vortex flow structures discussed above, the time periodic flow patterns are also of importance in a number of technological applications. Figure 7 gives the cross plane secondary flow at cross-sections $z = 0.3$ and 0.7 m ($Z \approx 10$ and 23.3) at three selected time instants in a periodic cycle for $Re = 51$ and $Gr/Re^2 = 65.3$ ($Gr = 1.7 \times 10^5$). The results clearly show the drastic time change in the flow structure at cross-section $z = 0.3$ m ($Z \approx 10$) at which the process of roll merging is taking place. While downstream at $z = 0.7$ m ($Z \approx 23.3$), the cell merging has completed and the roll pattern only experiences a mild change with time. Also note from the results that the experimental flow structure agrees only qualitatively with that from computation, although flow asymmetry is detected in both approaches. Besides, significant change in the vortex flow intensity with time is noted in the numerical results.

To further demonstrate the structural change in the vortex flow with the downstream distance, results for an even higher Gr/Re^2 at a given τ are shown in Fig. 8 for $Re = 51$ and $Gr/Re^2 = 96.1$ ($Gr = 2.5 \times 10^5$). The flow for this case is also time periodic with $\tau_p = 2.54$ [3] and only the instantaneous flow patterns at large τ are examined here. The experimental results clearly show that at this higher buoyancy-to-inertia ratio six

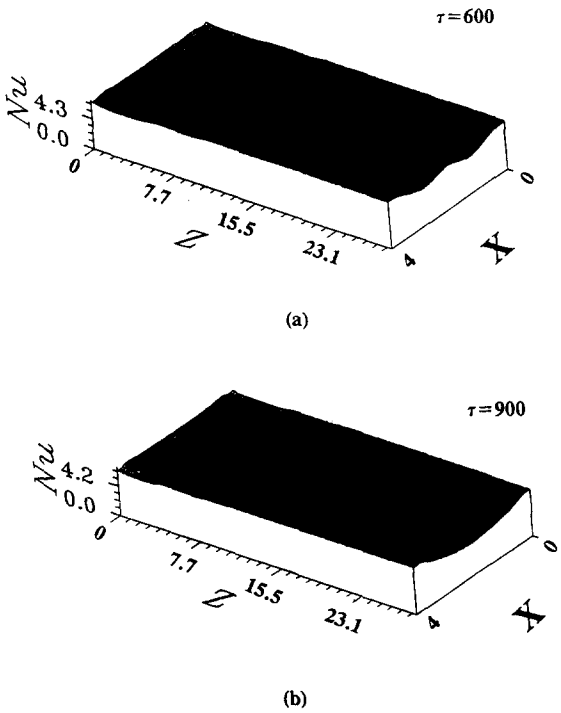

Fig. 9. The predicted local Nusselt number distributions on the heated bottom plate for $Re = 51$ for (a) $Gr/Re^2 = 65.3$ and (b) $Gr/Re^2 = 96.1$ at large τ.

asymmetric vortex rolls are induced in a shorter distance from the duct inlet, as evident from the photos for $z = 0.2$, 0.3 and 0.4 m ($Z \approx 6.7$, 10 and 13.3). But symmetric flow is predicted from the computation. It is important to note that the three pairs of vortex rolls quickly merge into one large nearly symmetric pair as the flow moves from $z = 0.4$ m to $z = 0.5$ m ($Z \approx 13.3$ to $Z \approx 16.7$). Further downstream, this one pair pattern remains unchanged. It is also important to note from the numerical results that the vortex flow intensity decays with the downstream distance for the three-pair pattern in the entry half of the duct. But the roll combination from three pairs to one pair over the section $z = 0.4$ to 0.5 m is found to greatly increase the vortex flow intensity. Additional results for the flow at high buoyancy with a different Gr/Re^2, which are not presented here due to the space limitation, also show the merge of the multiple vortex rolls into one or two large rolls in the exit half of the duct.

The distributions of the local heat transfer coefficient on the bottom heated plate are important in thermal design. Figure 9 presents the computed local Nusselt number distributions, defined as $Nu = hd/k = (d/k) \cdot [q''_w/(T_w - T_{in})] = 1/\theta_w$, for $Gr/Re^2 = 65.3$ and 96.1 for $Re = 51$ at τ, respectively, equal to 600 and 900. These distributions clearly reflect the instantaneous vortex flow structures. Specifically, in Fig. 9(a) we can see the heat transfer enhancement by the vortex flow and the dominated four roll structure in the second half of the duct, as discussed above. Furthermore, the roll generation and

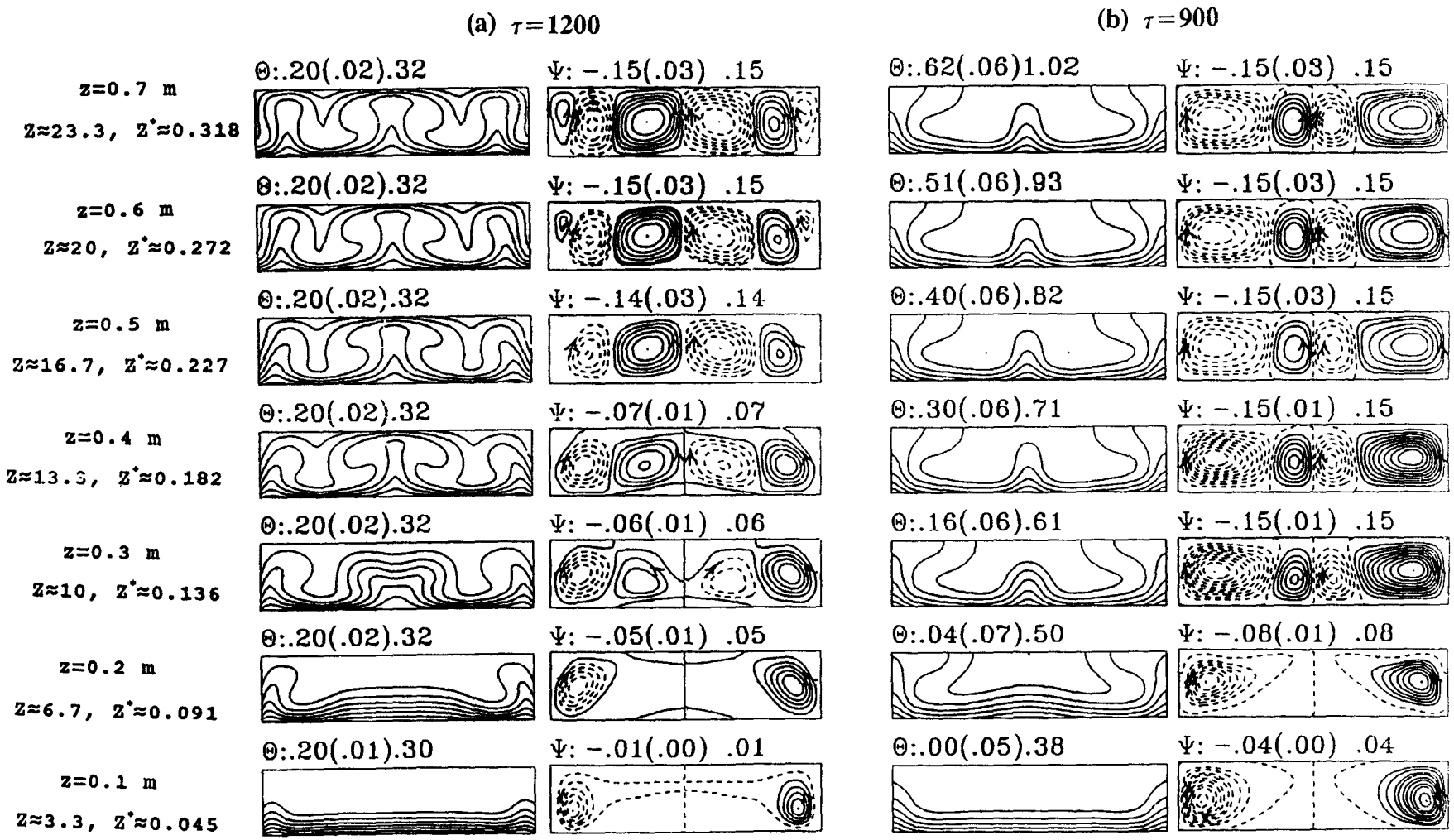

Fig. 10. Comparisons of the cross plane secondary flow from (a) conjugated analysis and (b) nonconjugated analysis for $Re = 102$ and $Gr/Re^2 = 2.4$ at selected cross-sections.

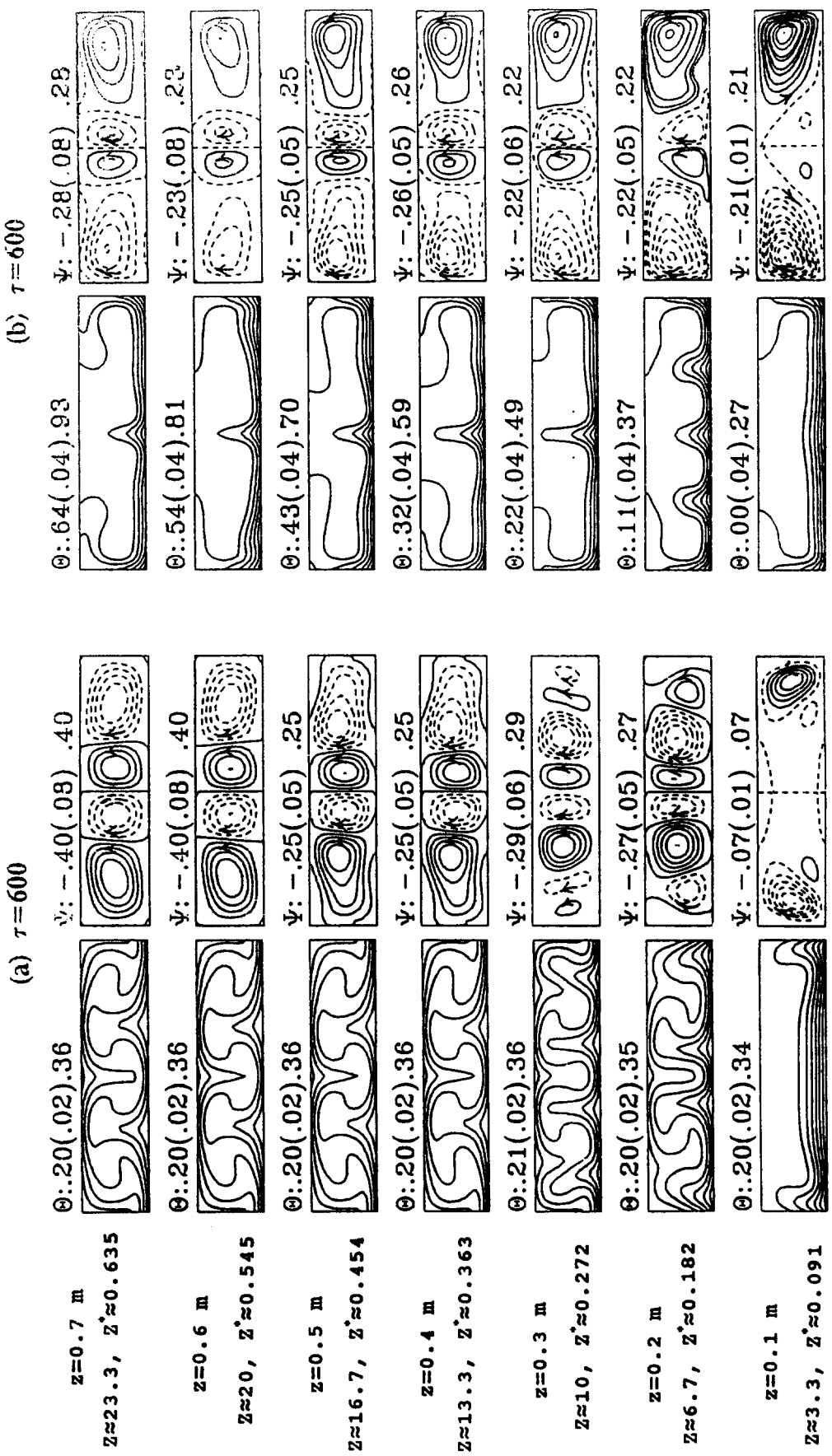

Fig. 11. Comparisons of the cross plane secondary flow from (a) conjugated analysis and (b) nonconjugated analysis for $Re = 51$ and $Gr/Re^2 = 65.3$ at selected cross-sections.

merging in the entry half can also be inferred from these results. At a higher buoyancy with $Gr/Re^2 = 96.1$, the result in Fig. 9(b) distinctly shows the drastic axial change in the roll structure and the prevalence of the two-roll pattern in the exit half of the duct.

4.2. *Importance of conjugated heat transfer*

Finally, the importance of the interactions between the convection in the flow and conduction in the solid walls on the vortex flow structure is illustrated by comparing the numerical results for those cases, including and excluding the conjugated effects. Figure 10 shows this comparison for the case with $Re = 102$ and $Gr/Re^2 = 2.4$ at steady state. These results indicate that there are significant differences in the thermal and flow structures predicted from the two different models. In particular, the nonconjugated analysis gives larger and stronger vortex rolls near the side walls and they circulate upwards along the side walls. These do not agree with the experimental observation. These unrealistic outcomes are mainly caused by the neglect of the conduction in the plexiglass side walls mentioned earlier, which then results in the heat input from the bottom heated plate accumulating in the bottom corners causing the bottom plate temperature near these corners to be much higher than that in another portion. Besides, the air is heated to a higher temperature, as clear from the values of the isotherms in Fig. 10(b). Including the side wall conduction, the conjugated analysis predicts the stronger and larger vortex rolls in the duct core and a third vortex pair is generated near the side walls in the exit region of the duct. This new vortex pair circulates downwards near the duct sides and is induced by the viscous shearing of the adjacent vortex rolls.

To further illustrate the conjugated heat transfer effects, comparison is also made in Fig. 11 for a flow with a higher buoyancy-to-inertia ratio for $Re = 51$ and $Gr/Re^2 = 65.3$. In addition to the differences discussed above for Fig. 10, the results in Fig. 11 show that the circulations of the vortex rolls predicted from the two models are in the opposite direction except in the section near the duct entry. Moreover, more vortices are generated in the flow in the section $z = 0.2$ to 0.3 m ($z \approx 6.7$ to 10) computed by the conjugated analysis.

The results from the present conjugated heat transfer analysis clearly manifest the importance of the conduction in the solid walls in affecting the buoyancy induced vortex flow evolution in an air flow. This is simply due to the thermal conductivity of air being much smaller than that of the solid walls.

5. CONCLUDING REMARKS

We have performed a combined experimental and three-dimensional unsteady conjugated heat transfer computation concerning the effects of the Reynolds and Grashof numbers on the axial evolution of the buoyancy induced secondary flow structures in a mixed convective air flow ($Pr = 0.72$) through a bottom heated horizontal rectangular duct ($A = 4$) by conducting instantaneous flow visualization, measuring time records of the air temperature and detailed numerical computation.

The results illustrated the generation of the vortex rolls in the entry region of the duct and the merging of the rolls downstream. More rolls are generated at a higher buoyancy-to-inertia ratio, and they merge into larger rolls. These experimentally observed vortex flow structures are in good agreement with the conjugated heat transfer analysis, except in the section where the vigorous roll merging is taking place. The conjugation of the conduction in the solid walls and the convection in the flow was shown to be rather significant in influencing the vortex structure of the air flow, and cannot be ignored in the analysis.

During the course of this study, it has been realized that the results obtained should be presented by certain generalized mixed convection parameter such as Gz, Gr_z/Re_z^2 or $Gr_z/Re_z^{1.5}$. These parameters, however are only appropriate for the high Reynolds number boundary layer flow and are not suitable for the low Reynolds number flow ($Re < 102$) considered here. A new generalized parameter remains to be found.

Acknowledgements—The financial support of this study by the engineering division of National Science Council of Taiwan, Republic of China through the contract NSC82-0404-E-009-141 is greatly appreciated.

REFERENCES

1. C. C. Huang and T. F. Lin, Buoyancy induced flow transition in mixed convective flow of air through a bottom heated horizontal rectangular duct, *Int. J. Heat Mass Transfer* **37**, 1235–1255 (1994).
2. C. C. Huang and T. F. Lin, Vortex flow and thermal characteristics in mixed convection of air in a horizontal rectangular duct: effects of the Reynolds and Grashof numbers, *Int. J. Heat Mass Transfer* **38**, 1661–1674 (1995).
3. W. L. Lin and T. F. Lin, Experimental study of unstable mixed convection of air in a bottom heated horizontal rectangular duct, *Int. J. Heat Mass Transfer* **39**, 1649–1663 (1996).
4. F. P. Incropera, Convective heat transfer in electronic equipment cooling, *J. Heat Transfer* **110**, 1097–1111 (1988).
5. G. Evan and R. Grief, A study of traveling wave instabilities in a horizontal channel flow with applications to chemical vapor deposition, *Int. J. Heat Mass Transfer* **32**, 895–911 (1989).
6. Y. Kamotani, S. Ostrach and H. Miao, Convective heat transfer augmentation in thermal entrance regions by means of thermal instability, *J. Heat Transfer* **101**, 222–226 (1979).
7. K. C. Chiu and F. Rosenberger, Mixed convection between horizontal plates—I. Entrance effects, *Int. J. Heat Mass Transfer* **30**, 1645–1654 (1987).
8. K. C. Chiu, J. Ouazzani and F. Rosenberger, Mixed convection between horizontal plates—II. Fully developed flow, *Int. J. Heat Mass Transfer* **30**, 1655–1662 (1987).
9. M. T. Ouazzani, J. P. Caltagirone, G. Meyer and A. Mojtabi, Etude numérique et expérimental de la con-

vection mixte entre deux plans horizontaux. *Int. J. Heat Mass Transfer* **32,** 261–269 (1989).
10. M. T. Ouazzani, J. K. Platten and A. Mojtabi, Etude expérimental de la convection mixte entre deux plans horizontaux à températures différents—II, *Int. J. Heat Mass Transfer* **33,** 1417–1427 (1990).
11. D. G. Osborne and F. P. Incropera, Laminar, mixed convection heat transfer for flow between horizontal parallel plates with asymmetric heating, *Int. J. Heat Mass Transfer* **28,** 207–217 (1985).
12. D. G. Osborne and F. P. Incropera, Experimental study of mixed convection heat transfer for transitional and turbulent flow between horizontal, parallel plates, *Int. J. Heat Mass Transfer* **28,** 1337–1344 (1985).
13. F. P. Incropera, A. L. Knox and J. R. Maughan, Mixed-convection flow and heat transfer in the entry region of a horizontal rectangular duct, *J. Heat Transfer* **109,** 434–439 (1987).
14. F. S. Lee and G. J. Hwang, Transient analysis on the onset of thermal instability in the thermal entrance region of a horizontal parallel plate channel, *J. Heat Transfer* **113,** 363–370 (1991).
15. K. C. Cheng and J. W. Ou, Convective instability and finite amplitude convection in the thermal entrance region of horizontal rectangular channels heated from below, *Proceedings of the Seventh Int. Heat Transfer Conference*, Munich, Paper NC-12, pp. 189–194 (1982).
16. F. C. Chou and G. J. Hwang, Voriticity-velocity method for the Graetz problem and the effect of natural convection in a horizontal rectangular channel with uniform wall heat flux, *J. Heat Transfer* **109,** 704–710 (1987).
17. H. V. Mahaney, F. P. Incropera and S. Ramadhyani, Development of laminar mixed convection flow in a horizontal rectangular duct with uniform bottom heating, *Numer. Heat Transfer* **12,** 137–155 (1987).
18. H. V. Mahaney, F. P. Incropera and S. Ramadhyani, Effect of wall heat flux distribution on laminar mixed convection in the entrance region of a horizontal rectangular duct. *Numer. Heat Transfer* **13,** 427–450 (1988).
19. R. K. Shah and A. L. London, *Laminar Flow Force Convection in Ducts*, pp. 196–198. Academic Press, New York (1978).
20. R. Peyret and T. D. Taylor, *Computational Methods for Fluid Flow*, Chap. 6. Springer, New York (1983).
21. T. Kawamura, H. Takami and K. Kuwahara, New higher-order upwind scheme for incompressible Navier–Stokes equations, *9th ICNMED*, Vol. 10, pp. 285–291 (1985).
22. C. Hirsch, *Numerical Computation of Internal and External Flow*, Vol. 1. pp. 176–179. Wiley, New York (1989).
23. D. A. Anderson, J. C. Tannehill and R. H. Pletcher, *Computational Fluid Mechanics and Heat Transfer*, pp. 71–77. Hemisphere, Washington DC (1984).